Flow-dependency aspects in SCAL of steady-state two-phase flow in model pore networks.

K. Mouravas[1,2], N. Karadimitriou[2], P. Dimitriadis[1], A. Giotis[3], M. Valavanides[1], H.Steeb[2]*

[1]Dept. of Civil Engineering, University of West Attica, GR-12244 Egaleo, Athens, Greece
[2]Institute of Applied Mechanics, University of Stuttgart, 70569 Stuttgart, Germany
[3]Dept. of Mineral Resources Engineering, Technical University of Crete, GR - 73100 Chania, Greece

Abstract. In the current phase of an ongoing study we systematically investigate the effects of pore network geometry and wettability on two-phase flow in porous media, aiming to address the limitations of traditional SCAL measurements. Microfluidic experiments are conducted in three distinct network types: transparent, planar, periodic and non-periodic PDMS networks, and periodic glass networks. This setup enables isolation and detailed analysis of individual physical effects. Taking advantage of the optical transparency of the planar models, a specialized imaging algorithm has been developed to monitor the spatio-temporal evolution of statistical flow properties during transient events, such as flow rate bump increments. The primary objective is to evaluate the establishment of fully developed flow conditions and to quantify the relationship between ex-core measurements, i.e. external pressure drops, and the internal flow architecture, particularly regarding the manifestation and magnitude of end-effects. By correlating these external observations with the interstitial structure of the flow, the work provides mechanistic insights critical for improving SCAL protocols. The ultimate aim is to generate flow-dependent relative permeability maps that are true to the underlying physics, thereby enhancing the specificity, reliability, and predictive accuracy of reservoir simulation models used in field applications.

1 Introduction

The phenomenology of steady-state two-phase flow in porous media is recorded in SCAL relative permeability diagrams. Conventionally, relative permeabilities are considered and expressed as functions of saturation. Yet, this has been put into challenge by theoretical, numerical and laboratory studies of flow in artificial pore network models and real porous media, that have revealed a significant dependency on the flow rates -especially when the flow regime is capillary to capillary/viscous, and part of the disconnected non-wetting phase remains mobile. These studies suggest that relative permeability models should include the functional dependence on flow intensities [1]. The explicit form of such dependence is valuable to the industrial applications community including the special core analysis area.

Recent laboratory studies invoking co-injection of two phases at steady state conditions through typical sandstone cores [2] and microfluidic pore network models [3], covering 4×4 orders of magnitude on the capillary number, *Ca*, and flowrate ratio, *r*, have verified that it is possible to extract an explicit expression relating the relative permeabilities to the flow intensities of the co-injected phases; that is especially so when the flow is fully developed. Moreover, through these experiments, specific physical characteristic invariants, such as the intrinsic dynamic capillary pressure curve, pertinent to the two-fluid and pore network system, were revealed in accordance to the inferences and predictions of the DeProF theoretical framework and extensive simulations [4,5].

The results of this on-going project indicate that the end-effects have a seemingly systematic -albeit latent- contribution to the flow structure – something expected. The contribution is substantial when the flow conditions are in the low *Ca* low *r* regime and also depends on the network geometry and wettability properties. A persistent problem is how we could assess the end-effects only from ex-core measurements, i.e. from conventional pressure drop measurements outside the core, without any information/image from the interstitial flow structure (e.g. saturation distribution).

To elaborate on this problem we expanded the systematic laboratory study to account for different network geometry and different wettability conditions. In a precursor study we have used periodic networks in PDMS material [3].

In the current study, in an attempt to decompose the effects of pore network geometry and wettability, we have repeated the microfluidic experiments in non-periodic microfluidic networks in PDMS material and periodic network geometry constructed in glass. To exploit the transparency of the microfluidic planar networks, we have also developed an imaging algorithm

* Corresponding author: marval@uniwa.gr

in order to evaluate the spatiotemporal evolution of statistical properties of the flow structure, especially during transients, e.g. flowrate bumps. The objective is to correlate the ex-core measurements with the interstitial flow structure and the extent of end-effects.

The scope of this on-going project is to improve SCAL protocols and in implementing true-to-mechanism (flow-dependent) relative permeability maps for developing simulators with improved specificity and predictive capacity.

2 Basic theoretical framework

Consider the simultaneous, one-dimensional concurrent flow of a non-wetting phase (NWP), and a wetting phase (WP), both incompressible. In the following, the variables pertaining to the NWP are indexed with *n*, whereas those pertaining to the WP are indexed with *w*. All variables are considered dimensionless; a tilde (~) is used to indicate a dimensional variable.

The two phases flow across a porous medium control surface, $\tilde{A}$, with flow rates $\tilde{q}_n$ and $\tilde{q}_w$ respectively. Average corresponding pressure gradients, $(\Delta\tilde{p}/\Delta\tilde{z})_i$, $i = n, w$, are induced upon the two phases. The term average refers to the representative elementary volume (REV) average. This type of two-phase flow is described by the set of phenomenological, fractional flow, Darcy-type relations,

$$\frac{\tilde{q}_n}{\tilde{A}} \equiv \tilde{U}_n = \frac{\tilde{k}}{\tilde{\mu}_n} k_{rn} \left(\frac{\Delta\tilde{p}}{\Delta\tilde{z}}\right)_n \quad \text{and} \quad \frac{\tilde{q}_w}{\tilde{A}} \equiv \tilde{U}_w = \frac{\tilde{k}}{\tilde{\mu}_w} k_{rw} \left(\frac{\Delta\tilde{p}}{\Delta\tilde{z}}\right)_w \tag{1}$$

where
$\tilde{U}_i$, $i = n, w$ are the superficial velocities,
$\tilde{k}$ the absolute permeability of the pore network and,
$\tilde{\mu}_i$, $i = n, w$ the dynamic viscosities of the two fluids.

The flowrate ratio, r, is defined as the ratio of volumetric fluxes,

$$r = \frac{\tilde{q}_n}{\tilde{q}_w} = \frac{\tilde{U}_n}{\tilde{U}_w} \tag{2}$$

and the mobility ratio, λ, is defined as the ratio of the phase mobilities,

$$\lambda = \frac{\tilde{\lambda}_n}{\tilde{\lambda}_w} = \frac{\frac{k_{rn}}{\tilde{\mu}_n}\left(\frac{\Delta\tilde{p}}{\Delta\tilde{z}}\right)_n}{\frac{k_{rw}}{\tilde{\mu}_w}\left(\frac{\Delta\tilde{p}}{\Delta\tilde{z}}\right)_w} = \frac{1}{\kappa}\frac{k_{rn}}{k_{rw}}\frac{\left(\frac{\Delta\tilde{p}}{\Delta\tilde{z}}\right)_n}{\left(\frac{\Delta\tilde{p}}{\Delta\tilde{z}}\right)_w} \tag{3}$$

where the NWP/WP bulk viscosity ratio is defined as

$$\kappa = \tilde{\mu}_n/\tilde{\mu}_w \tag{4}$$

The average intrinsic capillary pressure is [1, 3, 5]

$$\tilde{p}_c(\tilde{z}) \equiv \tilde{p}_n(\tilde{z}) - \tilde{p}_w(\tilde{z}) \tag{5}$$

where $\tilde{p}_i(\tilde{z}), i = n, w$, are the average bulk pressures in the NWP and WP respectively. Note, eqn. (5) provides a measure of the capillary pressure jump across the two bulk phase pressures; it is attributed to the combined effect of Young-Laplace capillary forces acting across all NWP/WP menisci.

2.1. Non-fully and fully developed flow

When the fluids are injected at constant flowrates, they switch from pure, fully saturated, independent, Poisseuille flow in tube to a complex network-flow mode whereby they interact with each other. Downstream the inlet ports the NWP disconnects into fluidic elements. Both NWP and WP create a flow system of some interstitial structure of evolving NWP size distribution. The local flow has a steady-state time average configuration; nevertheless this average configuration, changes – better, evolves or adapts – downstream. During this structural evolution the flow is considered to be *non-fully developed*. If the network, or the core, is adequately long and relatively homogeneous, then, far downstream the inlet ports, the flow system eventually abides to an invariant structure. In that case it is considered to be *fully developed*. Yet, settling into a fully developed structure is not always possible and depends on the flow conditions, as well as the properties of the fluids and the pore network. Amongst the many factors that regulate the evolution of the flow structure, most critical is the role of the relative magnitude of the viscous forces over capillary forces, and the length and homogeneity of the network.

Exhibits of interstitial flow transitions from non-fully developed to fully-developed structures can be found in [6], whereby two-phase flows within long Hele-Shaw bead packs have been studied.

As the two-fluid flow system evolves downstream into a fully developed structure, then the capillary pressure remains constant and the two pressure gradients pertaining to the NWP and the WP, become equal. Therefore, the phenomenological, fractional flow, Darcy type relations that describe the steady-state, fully developed flow, become

$$\tilde{U}_i = \frac{\tilde{q}_i}{\tilde{A}} = \frac{\tilde{k}}{\tilde{\mu}_i} k_{ri} \left(\frac{\Delta\tilde{p}}{\Delta\tilde{z}}\right) \quad , \quad i = n, w \tag{6}$$

and, under such conditions, the common pressure gradient in both phases can be expressed in reduced form

$$x = \frac{\Delta\tilde{p}/\Delta\tilde{z}}{(\Delta\tilde{p}/\Delta\tilde{z})^{1\Phi}} = \frac{\Delta\tilde{p}/\Delta\tilde{z}}{\tilde{\gamma}_{nw} Ca/\tilde{k}} = \frac{\Delta\tilde{p}}{\Delta\tilde{z}}\frac{\tilde{k}}{\tilde{\mu}_w \tilde{U}_w} = \frac{1}{k_{rw}} \tag{7}$$

where,
$(\Delta\tilde{p}/\Delta\tilde{z})^{1\Phi}$ is the pressure gradient corresponding to an equivalent saturated single-phase flow (1Φ) of the WP at the same superficial velocity $\tilde{U}_w$.
Ca is the capillary number, conventionally expressed as

$$Ca = \tilde{\mu}_w \tilde{U}_w / \tilde{\gamma}_{nw} \tag{8}$$

Note that, by definition, the reduced pressure gradient is essentially the inverse of the relative permeability of the WP [see far right side of Eq (7)].

Moreover, the set of superficial velocities in Eq. (6) may be appropriately reduced and replaced by a set of dimensionless variables, namely, the capillary number, Ca, Eq. (8), and the NWP/WP flow rate ratio, r, Eq. (2).

At steady-state conditions when the flow is fully developed, i.e. there are either no capillary end-effects or they can be considered to be negligible, the flow rate ratio, *r*, becomes equal to the mobility ratio, λ.

$$r = \frac{U_n}{U_w} \equiv \frac{1}{\kappa}\frac{k_{rn}}{k_{rw}} = \lambda \quad \Leftrightarrow \quad k_{rn} = \kappa r k_{rw} \qquad (9)$$

In fully developed flows, because of the common pressure gradient, Eqs. (6) or (7), and the equivalence between flowrate ratio and mobility ratio, Eq. (9), relative permeability curves intersect at a fixed value of the flowrate ratio, the so-called relative permeability cross-over value, r_x. The latter is equal to the inverse of the viscosity ratio,

$$r_x = 1/\kappa \qquad (10)$$

This inherent characteristic of steady-state, fully developed flows, Eqs. (9) and (10), may be used in assessing the presence of capillary end-effects when reviewing SCAL data. If the imposed flowrate ratio values, r_i, and the corresponding measured mobility ratio values, λ_i, are equal, then fully developed flow conditions have settled-in and end-effects are negligible. Ideally, in absence of end-effects, then, all pairs of $\{r_i, \lambda_i\}$ align on a straight line with inclination 1:1. Yet, in practice, when SCAL measurements are examined, the equality expressed by Eq. (9), could be used as a soft criterion in verifying the absence of end-effects. We have applied this criterion in the current study.

2.2. Energy efficiency & independent variables

The energy efficiency of the process, is considered as the flowrate of the NWP per unit of total hydraulic power spent, or equivalently, provided externally to the NWP/WP/PM system by the "pumps", to maintain two-phase flow at any set of externally imposed flow conditions, Ca and r. The associated *energy utilization factor*, or *energy efficiency index*, f_{EU}, can be readily calculated in terms of macroscopic measurements [1], as

$$f_{EU} = \frac{k_{rn}}{\kappa(r+1)} = \frac{r k_{rw}}{r+1} = \frac{r}{x(r+1)} \qquad (11)$$

An important characteristic of the sought process is that for every fixed value of the capillary number, Ca, there exists a single value of the flowrate ratio, r^*, for which the energy efficiency index, ${f_{EU}}^*$, attains a maximum value [1, 7]. Moreover, for every two-fluid/pore network system, a unique locus of energy efficiency maxima is formed, $r^*(Ca)$. The flow conditions that correspond to the $r^*(Ca)$ locus and minimize the total energy dissipation per unit of NWP flowrate, are called *critical flow conditions* (CFCs). The critical energy efficiency index, ${f_{EU}}^*(Ca)$, and the associated locus of CFCs, $r^*(Ca)$, provide a strong flow analysis and characterization tool [1].

2.3. Universal relative permeability scaling form, incorporating flowrate dependency

The mechanistic model *DeProF* (Decomposition in Prototype Flows) is a mechanistic framework for predicting the dimensionless macroscopic pressure gradient, x in immiscible, steady-state two-phase flow through pore networks. It integrates pore-scale interfacial dynamics and network-scale cooperative phenomena to stochastically estimate the effective conductivity of different pore unit cell classes. Utilizing effective medium theory and ensuring pore-to-macro-scale consistency for non-wetting and wetting phase mass transport, *DeProF* formulates an implicit algebraic expression linking x to key system and flow parameters: capillary number, Ca, flow rate ratio, r, viscosity ratio, κ, dynamic advancing and receding contact angles (θ_A, θ_R), and a parameter set, $\mathbf{x_{pm}}$, describing pore network geometrical and topological characteristics. Extensive simulations employing the *DeProF* model algorithm have mapped the flow regime dependencies across five orders of magnitude in Ca and r, for nine different viscosity ratios [4].

Based on the *DeProF* simulations it was possible to infer a universal description of the dependence of the reduced pressure gradient, $x(Ca, r)$, on the capillary number, Ca, and the flowrate ratio, r, expressed by the universal scaling form [5],

$$x(\log Ca, \log r) = A(\log Ca) + \kappa r \qquad (12)$$

The effects of capillarity and viscosity are partitioned in two decoupled terms. The linear term describes the fractional contribution of the bulk viscosities through the viscosity ratio, κ. The non-linear term, $A(\log Ca)$, accounts the contribution of capillarity at different flow conditions. That non-linear term, is the *Intrinsic Dynamic Capillary Pressure (IDCP)* function, and describes the capillarity effects associated to the physicochemical properties of the two-fluid system and the pore network, namely, wettability (dynamic receding and advancing contact angles) and pore network geometry. The relative contributions of those two terms depend on the flow conditions.

In particular, the *IDCP* function, $A(\log Ca)$, is a *characteristic property* of the NWP/WP/PM flow system. The term *dynamic* in IDCP is used to indicate that capillary pressure is evaluated at different flow conditions – not in static equilibrium [5].

In the present study we will perform a SCAL study and try to recover the IDCP, $A(\log Ca)$, specific to the two-fluids/pore network systems under consideration.

3 Materials and methods

The current SCAL study comprises simultaneous, continuous, steady-state, co-injections of two immiscible fluids within three different microfluidic networks, for a

range of flow conditions, organized in groups of constant, Ca values, covering an area of ~4 orders of magnitude on Ca and ~3 orders on r values, see Fig. 2.

3.1. Microfluidic model networks and fluids

Three model pore networks were used in the present study. Two networks were produced with Poly-Di-Methyl-Siloxane (PDMS) as the matrix structure and one network with glass.

All micromodels are planar (2D) and were produced in-house, implementing optical and soft lithography for the PDMS [8] and chemical etching [9] for the glass networks respectively. The pore structure of the median plane of the micromodels is exhibited in Fig. 1. For quick reference the codification of the network geometry is P for periodic and NP for non-periodic. The three networks are referenced by combining the attributes corresponding to the matrix material and the geometric characteristic, PDMS-P, Glass-P and PDMS-NP.

The basic geometric configuration of the three models is given in Table 1.

In the PDMS-P and Glass-P networks, Fig. 1, circles correspond to the mid-plane cross-sections of the PDMS cylinders (solid pillars) connecting the two parallel plates confining the flow. Both networks have exactly the same geometric structure on the median plane. The periodic structure is made by tiling-up a basic network element in both directions; 3 periods along the longitudinal axis (superficial flow direction), and 2 periods across the transverse axis. The depth of the porous structure in PDMS-P is uniformly equal to 43µm, constant throughout the entire pore space. The depth of the Glass-P is not uniform. The chemical etching process implemented on the two constituent glass plates creates eye-shaped pore cross sections combined with surface micro-roughness. Average depth gauges ~35µm.

In the PDMS-NP network, the irregular, closed contour geometric shapes ("islands") correspond to the mid-planar cross-sections of the PDMS upright prismatic objects (acting as solid pillars) connecting the two parallel plates confining the flow. The geometry is non-periodic and it is generated by an algorithm implementing spatial correlation models such as Gaussian or Exponential [9].

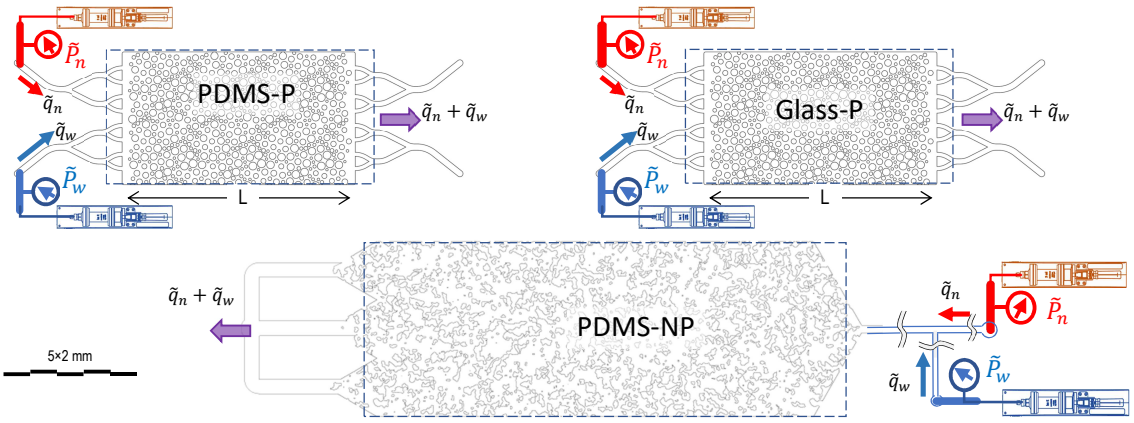

Fig. 1. Mid-plane section of the microfluidic networks (in-scale) used in the co-injection experiments and schematics of the constant displacement syringes. The fluids are co-injected through the inlet micro-channelling and the immiscible flow is collected at the exit. Top: the periodic (P) networks made of PDMS and glass; bottom: the non-periodic (NP) network made of PDMS.

Table 1. Basic geometric configuration of the three model networks used in the study

Network	PDMS-P	Glass-P	PDMS-NP
Length, $\tilde{L}$ [mm]	20	20	38
Width [mm]	10	10	13
Depth [µm]	43	~35	56
Abs. Permeability, $\tilde{k}$ [m^2]	8.10×10^{-11}	1.29×10^{-11}	1.61×10^{-11}

The fluids used in the study were deionized water dyed with ink, and Fluorinert™ FC-770. The basic physicochemical and wettability properties of the fluids are presented in Table 2.

Wettability of the two-fluid and PDMS / Glass system is described by the dynamic advancing and receding contact angles, with nominal values roughly estimated from visual observations of the recorded snapshots at $\theta_A = 54 \pm 5$ deg and $\theta_R = 45 \pm 5$ deg respectively.

Table 2. Basic physicochemical properties and wettability of the pair of fluids used in the study

Fluid	Density $\tilde{\rho}$ [kg/m^3]	Dynamic viscosity $\tilde{\mu}$ [mPas]	Interfacial tension $\tilde{\gamma}_{nw}$ [N/m]	Solid	
				PDMS	Glass
Fluorinert™ FC-770	1793	1.359	55×10^{-3}	WP	NWP
Deionized Water + Dye	1000	1.00		NWP	WP

3.2 Experimental set-up and procedure

The experimental set-up was already used in a precursor study [3]. The two fluids were co-injected independently at predetermined volumetric fluxes, using two CETONI™, neMESYS 1000N, syringe pumps, combined with a BASE120 module. Inlet pressures per phase were measured with a set of Elveflow™ MPS sensors, depending on the values of the expected pressure build-up during the injection and the desirable /acceptable measurement accuracy. Both syringe pumps, and logging of the pressure readout values were controlled with QMixElements™. Sampling and recording of the pressure values at the inlet port for each phase was set at rates between 0.5 and 10 Hz, depending on the flow conditions and the expected speed of events.

In order to assess whether or not the process has reached interstitially steady-state, the entire flow system was visualized using an open-air microscope, with a monochromatic camera, Basler™ 5 Mpx, 23 fps, acA2440-20gm. The purpose of visualizing the interstitial flow was for cross-checking between the structure of the flow, the read-outs from the pressure transducers, and the injected fluxes. There was no video recording but simple snapshot capturing at a frame rate from 15 to 1 Hz, and at a resolution around 8μm/pixel, adequate to observe pore-scale events. Indicative, compressed snapshots are presented in Fig. 4 for two co-injection experiments at $Ca = 3.463 \times 10^{-6}$ and $Ca = 8.225 \times 10^{-5}$ in the Glass-P model network, whereby the WP (Deionized Water + Dye) is black, and the NWP (Fluorinert™ FC-770) is white (transparent)

Procedure followed for each *experiment* – With the term "experiment" we refer to a complete cycle of co-injecting the two phases, at constant WP volumetric flowrate but with successive increases of the NWP flowrate. The protocol followed was identical to that of the precursor study [3]. For every experiment a fixed capillary number value, Ca_i, is maintained, whereas the flowrate ratio takes successive step-up values, r_j.

The domain of flow conditions in the entire set of experiments is depicted in Fig. 2. A total of 44 constant-Ca experiments were performed; 13 in the PDMS-P, 19 in the Glass-P and 12 in the PDMS-NP model networks.

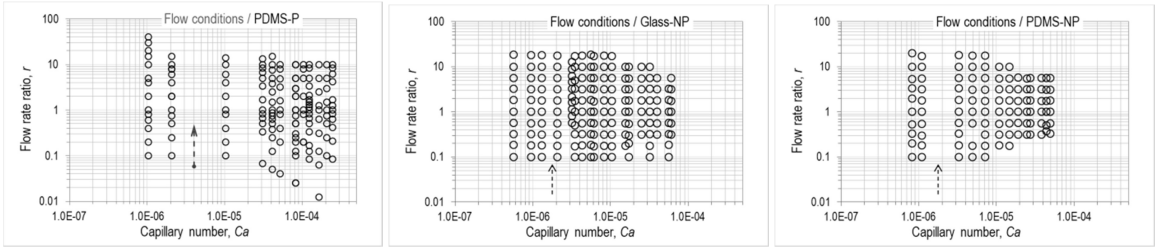

Fig. 2. The domains of steady-state flow conditions examined in the study. Markers indicate values of the capillary number, $\boldsymbol{Ca_i}$, and flow rate ratio, $\boldsymbol{r_j}$. The dashed arrow indicates the direction of increase of the flowrate of the NWP (at fixed $\boldsymbol{Ca_i}$) for all experiments.

The typical cycle in every experiment comprise the following interventions:

The micromodel is initially saturated with the wetting phase. Then, both phases are injected into the network.

The WP is injected at a fixed volumetric flowrate in order to maintain a constant value of the capillary number, Ca_i, during the entire cycle of the experiment.

The volumetric flowrate of the NWP starts at ~1/10 of the WP flowrate and it is increased in successive steps (about 9 to 12) to 10 times larger; the result is ~3 orders of magnitude in successive increments. After each step-up of the NWP flowrate, an adequate period of time is allowed for the interstitial flow to reach steady-state.

As soon as the time-averaged pressure values show signs of stabilization for both phases (kinetic stabilization), the entire network is visually inspected to cross-check that the interstitial flow has also stabilized, or any fluctuations show some kind of sustainable, short-cycle periodicity. In most of the cases, a steady value for the pressures would come along with a stabilized flow, judging from visual inspection of the interstitial flow (changes in saturation, migration of menisci, other pore-scale phenomena). Following the setting of steady-state conditions in the interstitial flow, the volumetric flowrate of the non-wetting phase is stepwise increased.

After successive repeats with progressive stepwise increments of the flowrate of the NWP, corresponding to a flowrate ratio value, of at least $r = 10$, the experiment for that particular constant-Ca value stops.

The system is then reconfigured and a new cycle is deployed pertaining to a new Ca value.

The protocol described above was repeated for the experiments in the three model networks.

3.3 Data logging and management

For each run at constant $\tilde{q}_n$ and $\tilde{q}_w$ the values of flow rates and gauge pressures at the inlet ports for each phase, were sampled at predetermined rates and recorded (see previous subsection). The recorded data were graphically plotted. Endpoint (steady-state) pressures were estimated from these plots by time averaging.

Typical evolution of the two flowrates and pressures at the inlet ports are exhibited in Fig. 5, top diagram. After the stabilization of the flow occurring at the NWP flowrate step-ups, the pressure values are calculated by time averaging over a selected interval. Delimiting this time interval for every examined flow set-up, (Ca, r), follows after identifying some form of stabilization in the corresponding pressure logging diagram. Then, the

average endpoint (steady-state) pressures $\langle\tilde{P}_n\rangle, \langle\tilde{P}_w\rangle$, are automatically calculated by simple averaging over the corresponding time interval. The pressure gradients for the WP and the NWP are then readily calculated as

$$(\Delta\tilde{p}/\Delta\tilde{z})_i = \langle\tilde{P}_i\rangle/L \ , \quad i = n, w \tag{13}$$

The middle and bottom diagrams in Fig. 5 exhibit a typical evolution of primary statistics (mean, cumulative mean, standard-deviation, skewness) and selected probabilities of the grayscale intensity for each recorded frame pertaining to the entire Glass-P model network for the whole experiment of steady-state co-injection at $Ca = 8.225 \times 10^{-5}$.

4 Results

The pair of pressure gradient values per phase, $\{(\Delta\tilde{p}/\Delta\tilde{z})_n, (\Delta\tilde{p}/\Delta\tilde{z})_w\}$, was used to calculate the corresponding pair of relative permeability values for the NWP and WP, $\{k_{rn}, k_{rw}\}$, from Eq. (6).

We need to stress here that we have considered the general condition that the flow may not be fully developed, therefore the NWP and WP pressure gradients would not be necessarily equal. In such general condition, $(\Delta\tilde{p}/\Delta\tilde{z})_n \neq (\Delta\tilde{p}/\Delta\tilde{z})_w$, therefore

$$k_{rn} = \tilde{\mu}_n\tilde{U}_n/\left[\tilde{k}\left(\frac{\Delta\tilde{p}}{\Delta\tilde{z}}\right)_n\right] = \tilde{\mu}_n r\tilde{U}_w/\left[\tilde{k}\left(\frac{\Delta\tilde{p}}{\Delta\tilde{z}}\right)_n\right]$$
$$k_{rw} = \tilde{\mu}_w\tilde{U}_w/\left[\tilde{k}\left(\frac{\Delta\tilde{p}}{\Delta\tilde{z}}\right)_w\right] \tag{14}$$

Pairs of NWP and WP relative permeability values $\{k_{rn}, k_{rw}\}$, were calculated using Eq. (14). The collected relative permeability values were plotted against the corresponding values of the flowrate ratio, r, into diagrams pertaining to into diagrams pertaining to the 44 constant-Ca experiments. Due to space limitations only diagrams pertaining low (10^{-6}), mid (10^{-5}) and high-Ca (5×10^{-6}) experiments are presented in Fig. 3.

In the same diagrams we have also plotted values of the energy efficiency, f_{EU}, Eq. (18).

To test if the flow is fully-developed we have also plotted the mobility ratio values, λ, Eq. (3), pertaining to the relative permeability values obtained from Eq. (14), against the flowrate ratio r.

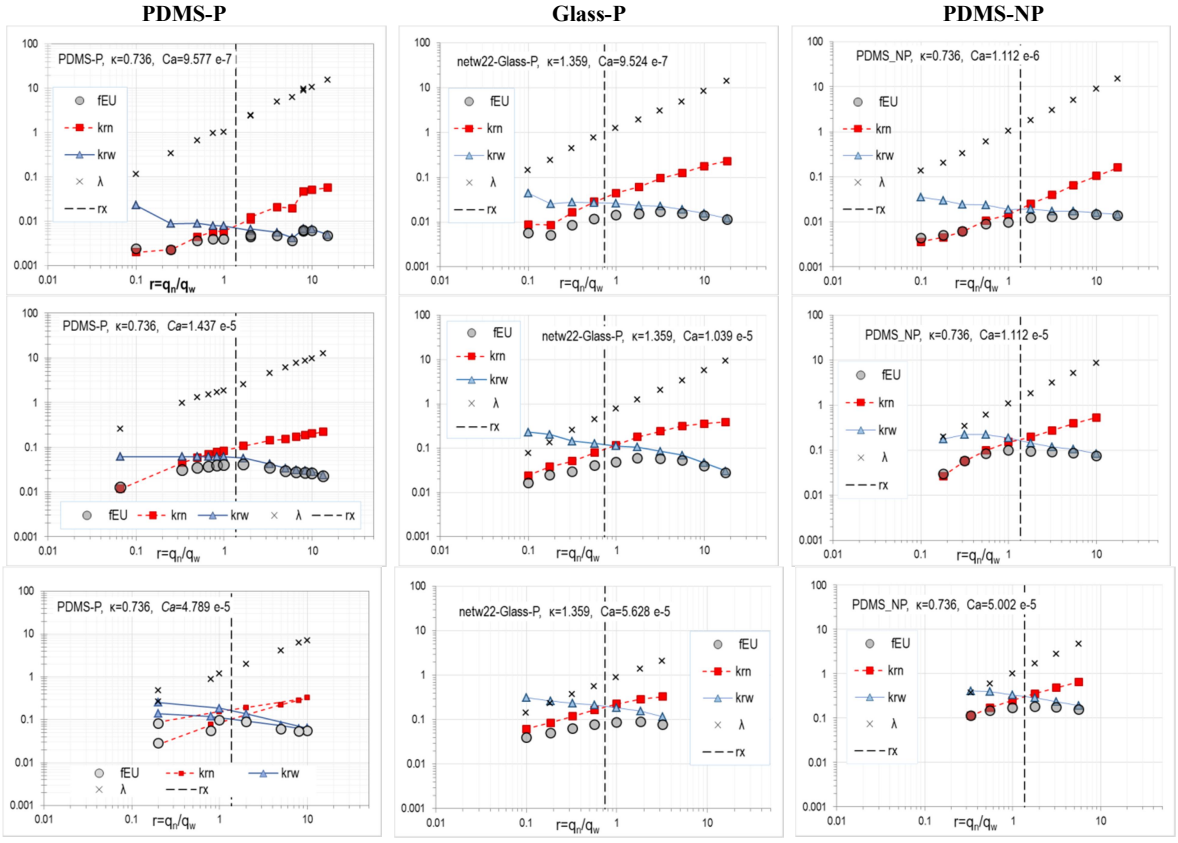

Fig. 3. Indicative diagrams of relative permeability for NWP and WP (■ k_{rn}, △ k_{rw}), energy efficiency, f_{EU} (○), and mobility ratio, λ (×) in terms of flowrate ratio, r. Diagrams on the same column pertain to co-injections within the same pore network. Diagrams on the same row pertain to similar Ca values, i.e. 10^{-6} (top row), 10^{-5} (middle row) and 5×10^{-5} (bottom row). Each diagram is associated to successive runs under constant- Ca value. The straight, dashed, vertical lines indicate the theoretical value of the relative permeability cross-over flowrate ratio value, as predicted by Eq. (10).

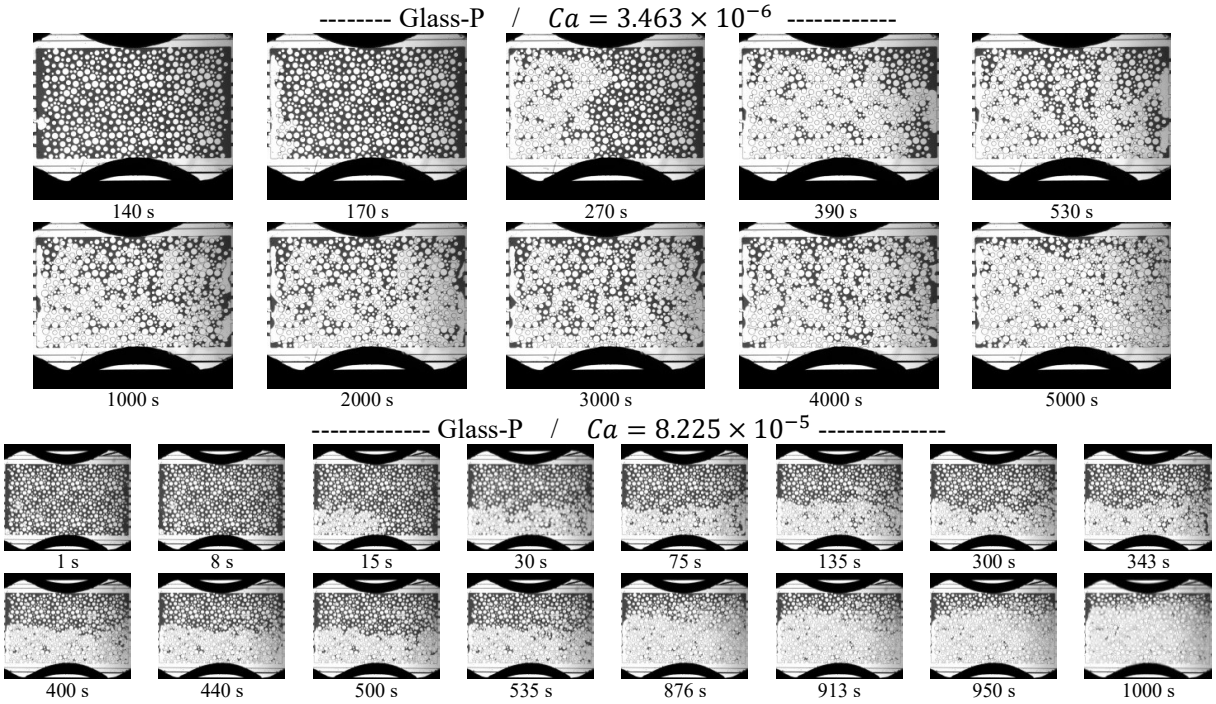

Fig. **4**. Selected snapshots pertaining to steady-state co-injection within the Glass-P model network, at $Ca = 3.463 \times 10^{-6}$ (140-500 s) and $Ca = 8.225 \times 10^{-5}$ (1-1000s). WP is black, NWP is white (transparent). Numbers indicate time lapse from injection start.

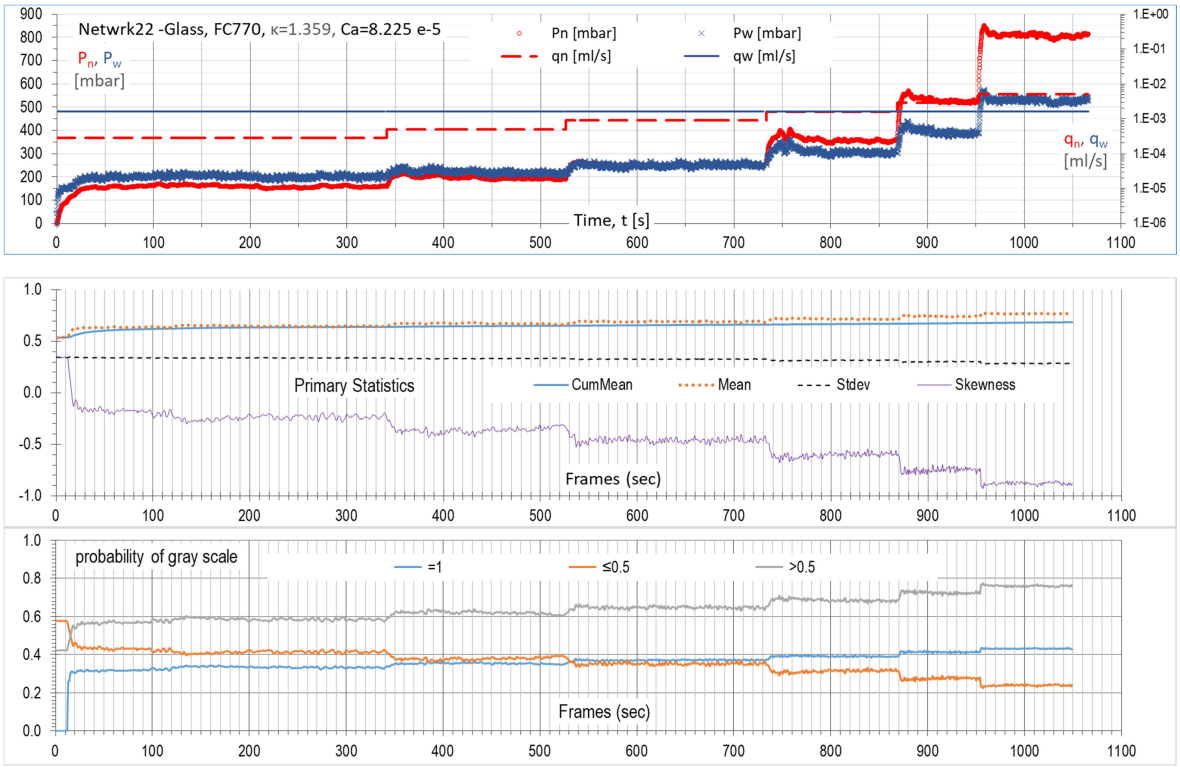

Fig. 5. Time evolution diagrams pertaining to the entire experiment of steady-state co-injection at $\boldsymbol{Ca = 8.225 \times 10^{-5}}$ in the Glass-P model network. **Top** – The measured pressures at the inlet ports are indicated by the small circle markers (red, ○) for the NWP; and by the small cross markers (blue, ×) for the WP; the compact line (blue, ⟝) indicates the WP volumetric flow rate, $\tilde{q}_w$ dashed line (red, ⟝ ⟝) for the NWP, $\tilde{q}_n$. **Middle** –Time evolution of the grayscale intensity primary statistics (mean, cumulative mean, standard-deviation, skewness) for each recorded frame pertaining to the entire network. **Bottom** – Selected probabilities of the grayscale intensity for each recorded frame.

4.1 Relative permeability scaling incorporating flowrate dependency

We proceed with revealing the flow dependent relative permeability scaling for the steady-state two-phase co-injections in the three microfluidic pore networks.

Considering the flow is fully developed, we calculated the reduced pressure gradient, $x = 1/k_{rw}$, i.e. the inverse of the relative permeability of the WP using Eq. (7). The entire set of x values is plotted in terms of the flow rate ratio, r, in the top-row diagrams and in terms of the capillary number, Ca, in the bottom-row diagrams in Fig. 6.

In particular, the values of reduced pressure gradient, x, are displayed in terms of log$r$, in groups of constant-Ca values. Please note that, with increasing r, there is an obviously systematic, asymptotic trend in aligning to the dashed, inclined line towards a virtually decoupled flow state. That is described by

$$\text{As } r \to \infty, \quad \log x = \log \kappa + \log r \;\Leftrightarrow\; x = \kappa r \qquad (15)$$

The inclination of the dashed line in the three log-log, top-row diagrams in Fig. 6, is equal to 1:1, and its pivot (marked by ○) is located at $\{1, \kappa\}$.

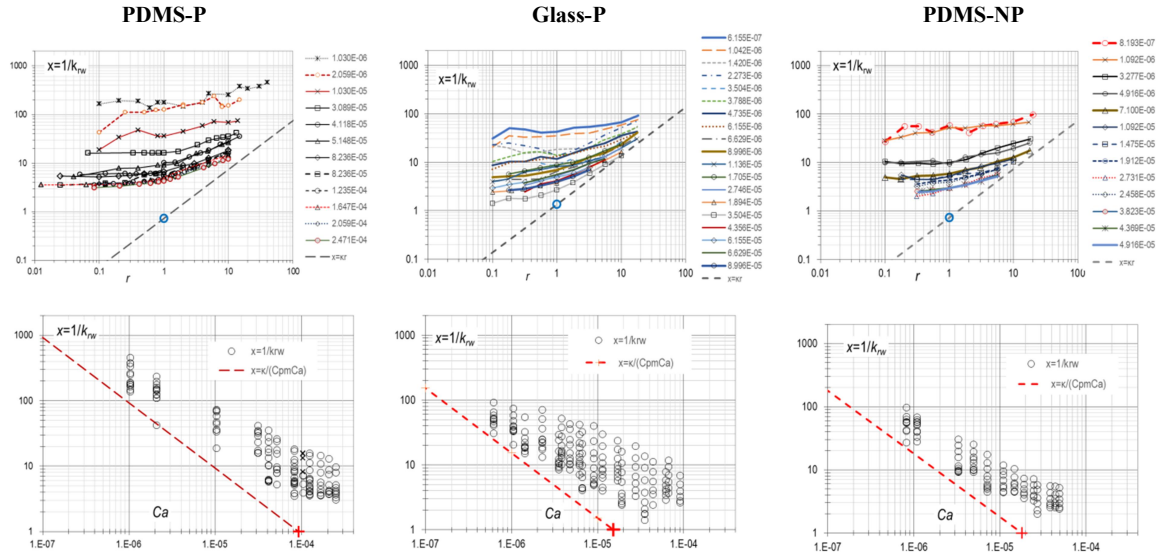

Fig. 6. Reduced pressure gradient (inverse WP relative permeability) values in terms of $\boldsymbol{r}$ for constant $\boldsymbol{Ca}$ values (top row), reduced pressure gradient values in terms of $\boldsymbol{Ca}$ for different $\boldsymbol{r}$ values (middle row), for the three NWP/WP/PM systems examined in the study (periodic networks PDMS-P, left column, Glass-P, centre column, and non-periodic networks PDMS-NP, right column).

In the bottom-row diagrams in Fig. 6, the values of reduced pressure gradient, x, are displayed in terms of $\log Ca$, and lined-up in vertical rows of constant Ca. Within the same row, markers depict different values of the flow rate ratio, r. Note here: as we did not run all experiments on the same flow rate ratio values, it was not possible to group the x-values into r-classes.

Although not quite obvious, there is a tendency (a confluence) of the markers to converge and align – in an asymptotic manner – towards the inclined, dashed line (in red). The trend is described by

$$\log Ca \ll 0, \log x = \log \kappa - \log C_{pm} - \log Ca$$
$$\Leftrightarrow x = \kappa/(C_{pm} Ca) = 1/(Ca_{pm} Ca) \qquad (16)$$

The functional form of this asymptote is given by an expression, up to a constant value, C_{pm}, associated to the NWP/WP/PM system [5]. The line asymptote has a negative inclination equal in measure to 1:1. For the available set of data displayed in the bottom row diagrams, we have used arbitrary, best-guess, constant values $\log C_{pm}$, to pivot the line along the Ca axis at $Ca_{pm} = \kappa/C_{pm}$. By increasing these values but keeping the negative inclination equal to 1:1, the lines are transferred in parallel to the left, at lower Ca pivot points, and vice versa. To estimate the C_{pm} values more precisely, we need to have more data and, most importantly, the data should pertain to capillarity dominated flows, i.e. to flows at high Ca values, close to the data markers confluence region. The recovery of the correct C_{pm} value for a certain system is essentially a "dynamic network-typing" (as in "dynamic rock-typing") procedure. That is because the value of C_{pm} is associated to the interaction between the structure of the pore network and the wettability of the two-fluid system against the network surface – the dynamic advancing and receding contact angles.

The trend in the diagrams in Fig. 6 is similar to the trend observed in the *DeProF* model simulations [5] pertaining to a virtual sandstone network model. The same trend is observed in a similar diagram, pertaining to the lab study on a natural sandstone core [2]. We need to remind here that the inclined asymptotes describe or,

better, delineate, the domain of flow conditions whereby the compound flow resistance, attributed entirely to the bulk phase viscosities, is partitioned on complementary volume fraction rations, namely, saturation. And it is only at those high flowrate conditions (high-Ca) that relative permeabilities can be expressed in terms of saturation in a "saturation-dependency" fashion. A similar trend is observed in the very low-Ca regime (capillarity dominated flows); nevertheless that trend is a bit fuzzy as it depends strongly on the distribution of the menisci of the stranded ganglia within the network.

In order to describe the steady-state two-phase flow in the particular microfluidic system, in the form of the universal scaling function Eq. (12), we need to reveal the associated kernel function, $A(\log Ca)$, namely the Intrinsic Dynamic Capillary Pressure (IDCP) curve [5]. To this end we have implemented the fitting procedure described in [3].

In the diagrams in Fig. 7, we plot the A_i values calculated in terms of Ca_i, via Eq. (12). The small black circles mark the IDCP values, A_{ij}, per r_j, aligned into rows of constant-Ca_i groups. Average values of $A_i = \langle A_{ij} \rangle$ per constant-Ca_i are marked with large red circles. These are fitted by a power law (red dashed curve),

$$\log A = aCa^{-b} \tag{17}$$

The power law indicates that, asymptotically, as $Ca \to \infty$, $A(\log Ca)$ decays to 1, therefore Eq. (12) becomes $x \to 1 + \kappa r$, and the saturation dependency is recovered, yet in an asymptotic fashion, for the viscous flow regime. The values of the fitting coefficients a, b are exhibited in Table 3.

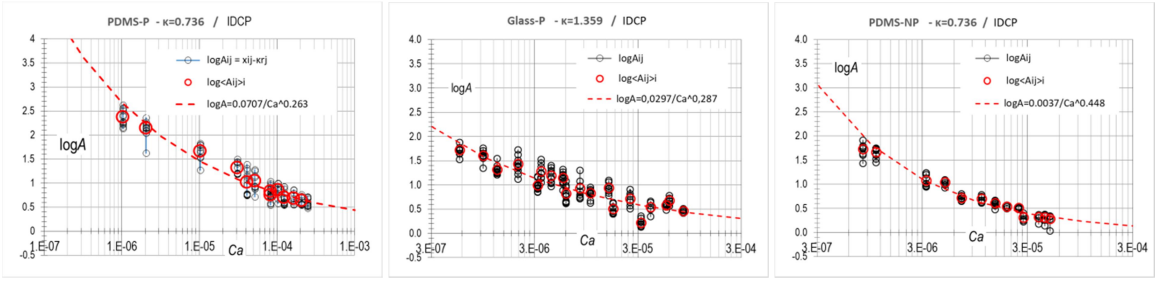

Fig. 7. Intrinsic Dynamic Capillary Pressure function, $\boldsymbol{A(Ca)}$, Eq. (12), in terms of the capillary number $\boldsymbol{Ca}$

Table 3. Power law fitting coefficients of the IDCP curve for the two-fluid/network systems examined in the study

Coefs \ System →	PDMS-P	Glass-P	PDMS-NP
a	0.0707	0.029	0.0037
b	0.263	0.287	0.448

The standard deviations of the A_{ij}, values per constant-Ca_i, can be weighted-in to the square of errors to improve the power law fitting.

4.2 Energy efficiency & critical flow conditions

Energy efficiency analysis is a complementary method to reveal any latent systematic trends and get a better image of the interstitial flow structure within the two-fluid/pore network systems examined in the study.

We have calculated the energy efficiency values based on the same structure as of the original /nominal expression, Eq. (11), but instead using the flowrate ratio, we used the mobility ratio, λ, therefore

$$f_{EU} = \frac{\lambda k_{rw}}{\lambda + 1} \tag{18}$$

In that context, the interstitial flow was described by the *kinetic* [Eq. (18)] rather than the *kinematic* [Eq. (11)] definition of the energy efficiency index.

The compound diagrams in Fig. 8 provide the results of the energy efficiency analysis, implementing Eqs. (11) and (18), as described in [1]. In particular, the diagrams in Fig. 8, display two sets of data.

Focusing on the lower part of the diagrams in Fig. 8, sets of small hollow circles indicate the values of energy efficiency, $\{r_j, f_{EU,ij}\}$ per constant-Ca_i experiment (with reference to the collection of diagrams in Fig. 3).

For every constant-Ca_i experiment, a maximum value is detected from the energy efficiency values, $f_{EU,ij}$, as

$$f^*_{EU,i} = f^*_{EU}(Ca_i) = \max_j \{f_{EU,ij}, Ca_i\} \tag{19}$$

These maximum values are marked by larger, filled circles. A remarkably smooth increase of the maximum energy efficiency values, f^*_{EU}, with increasing Ca, is observed. Moreover, depending on the flow conditions, the maximum energy efficiency of the process may increase by 2 orders of magnitude. Operation-wise, that is a quite important characteristic when designing this type of processes. The maximum values (filled circle markers) tend to reach a maximum value – the, so called, "ceiling of efficiency" [1], that is given by

$$f^*_{EU\infty} = \left(1 + \sqrt{\kappa}\right)^{-2} \tag{20}$$

Refocusing on the upper part of the of the compound diagrams in Fig. 8, sets of markers indicate the so-called,

critical flow conditions (CFCs), pertaining to the detected local maxima per constant-Ca_i experiment

We may recall here the definition of critical flow conditions, as the conditions whereby the flowrate of the NWP per unit of hydraulic power necessary to maintain the mixed flow takes maximum values [1]. This is evaluated in appropriately reduced form by the energy efficiency index, Eq. (18). In that context, CFCs are identified by observing the maximum values of the energy efficiency $f^*_{EU,i} = f^*_{EU}(Ca_i)$, Eq. (19).

On the diagrams in Fig. 8, both critical flowrate ratio, r_i^*, and mobility ratio, λ_i^*, are plotted in terms of $\log Ca$. A discrepancy between r_i^* and λ_i^*, is pronounced in the low-Ca domain, i.e. at capillarity dominated flow regimes, while it is insignificant at the high-Ca domain where bulk viscosity prevails and the effect of menisci is practically negligible. The detected CFCs show a trend similar to an S-curve. The trend is a bit fuzzy in the low-Ca regime, so we calculated the log-averaged values as

$$\log \hat{r}^* = (\log r^* + \log \lambda^*)/2 \;\Rightarrow\; \hat{r}^* = \sqrt{r^* \lambda^*} \qquad (21)$$

These values are marked on the CFC diagrams using red, upright cross markers (+). The CFCs markers will be fitted by a 4 parameter S-curve

$$\log \hat{r}^* = \log r_\infty^* + \frac{\log r_0^* - \log r_\infty^*}{1 + exp[(\log Ca - \log C)/z]} \qquad (22)$$

where:

$\log r_\infty^*$ and r_0^* are the critical flowrate values at the viscous (very high Ca) and capillary (very low Ca) regimes respectively, and form the two parallel asymptotic boundaries of the S-curve;

$\log C$ is the $\log Ca$ value for the curve point that is midway between $\log r_0^*$ and $\log r_\infty^*$;

z is the corresponding inclination of the curve.

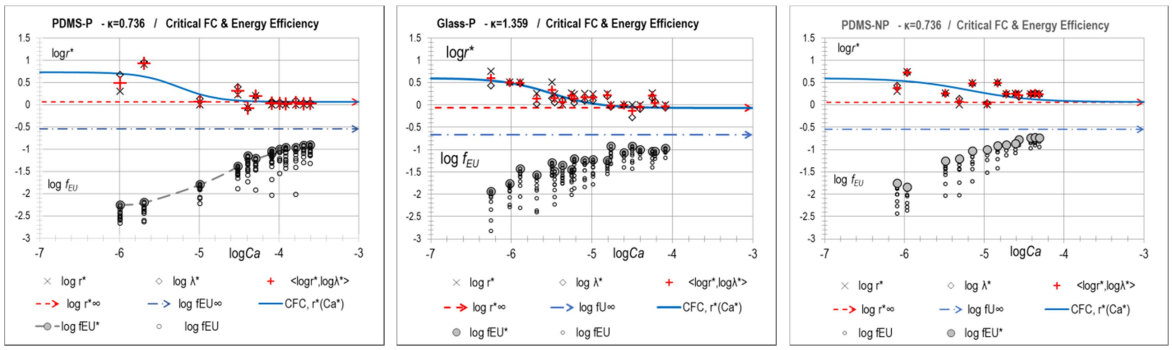

Fig. 8. Energy efficiency values $\{r_j, f_{EU,ij}\}$, ○, and detected maximum values $\{Ca_i, f^*_{EU,i}\}$, ⊙, for the three systems examined in the study (PDMS-P, Glass-P and PDMS-NP). The corresponding critical flow rate ratio values, $\{Ca_i, r_i^*\}$, ×, and mobility ratio values, $\{Ca_i, \lambda_i^*\}$, ◇, define the so-called Critical Flow Conditions; upright cross markers in red, +, indicate the mean of the flow rate ratio and mobility ratio values, $\hat{r}^*$, Eq. (21).

On the diagrams in Fig. 8, the dashed red, horizontal line indicates the nominal value of the critical flow rate ratio for pure viscous flow conditions (as $Ca \to \infty$). Given the viscosity ratio of the two fluids, κ, the theoretical (nominal) value of the critical flowrate ratio for pure viscous flow conditions [1] is estimated as

$$r_\infty^* = 1/\sqrt{\kappa} \qquad (23)$$

The values of the fitting parameters, Table 4, are estimated by minimizing the sum of the squared fitting errors. These can be used as the identity of each two-fluid/pore network system ("rock typing").

The actual value attained within the lower part of the S-curves, pertaining to larger Ca values, indicates an asymptotic trend, that is remarkably close to the theoretically predicted value, r_∞^*, Eq. (23). Moving on to the low-Ca regime (capillary flows) the observed fuzziness in locating the CFCs is attributed to significant capillary end-effects.

Table 4. Characteristic parameter values for the three two-fluid/pore network systems examined in the study.

Parameter	PDMS-P	Glass-P	PDMS-NP
$\log f^*_{EU\infty}$	-0.538	-0.671	-0.538
$\log r_\infty^*$	0.0666	-0.067	0.067
$\log r_0^*$	0.7328	0.600	0.600
z	0.2450	0.300	0.400
$\log C$	-5.2522	-5.513	-5.197

Comparing the S-curves for the CFCs in the two-fluid/pore network systems examined (ref. Fig. 8 & Table 4) we observe that the transition from capillary to viscous flow is smoother (over a broader Ca region) in the PDMS-NP system ($z_{Glass} < z_{PDMS-NP}$) and the shift takes place at a larger Ca value ($\log C_{Glass-P} < \log C_{PDMS-NP}$). Overall, the trend across the three two-fluid/pore network systems examined is systematic. There are conceptual similarities to the diagrams furnished in the theoretical framework [1], and also to

the diagrams produced in a recent SCAL study [2] on a natural core across a broad domain of flow conditions.

4.3 Paradigms of application in SCAL

The proposed relative permeability scaling model, accounting for flowrate dependency, together with the background theoretical framework (analysis of energy efficiency, critical flow conditions etc.) have potential applications in SCAL and reservoir engineering.

A central problem in SCAL is handling non-fully-developed flow conditions or the presence of capillary end-effects. Fully developed flow is not a condition always attained in SCAL measurements. The evolution of the interstitial flow until fully developed flow conditions are established depends on the structure of the pore network, the wettability of the two-fluid/solid system and the superficial velocity of each fluid. In general, end-effects are pronounced when capillarity-associated phenomena are not suppressed by viscous resistances. The analysis presented in the current study can be applied in SCAL. Taking ex-core measurements and implementing a few checks, some simple, e.g. comparing the imposed flowrate ratio vs the measured mobility ratio, and some a bit more complicated, e.g. energy efficiency analysis in terms of flow conditions, it is possible to detect/assess the presence of end-effects, characterize the pore network ("rock typing"), etc.

As a paradigm, in assessing the degree to which the co-current flows in the different networks have reached a fully-developed structure, we may focus on the diagrams in Fig. 3, Note that the markers (×) indicating values of the mobility ratio, λ_i, against, r_i, are – in general – aligned along a straight line with gradient 1:1. In many cases, the two values are practically equal, i.e. $\lambda_i = r_i$. For those cases, the kinetic states of the interstitial flow structures, λ_i, are consistent to the externally imposed, kinematic constraints, r_i, indicating that the corresponding flows are fully developed. Yet, in some diagrams, we may observe some degree of discrepancy between the mobility ratio and the flowrate ratio, manifested as a failure of the $\{\lambda_i, r_i\}_{Ca}$ markers to perfectly align to the $r = \lambda$ straight line. That means that the co-injections that are misaligned might have not reached a fully-developed interstitial structure. We may evaluate the degree of misalignment by calculating the Pearson correlation coefficient between the set of λ_i, r_i pairs per Ca. The results for all the constant- Ca experiments in the three systems are presented in Fig. 9.

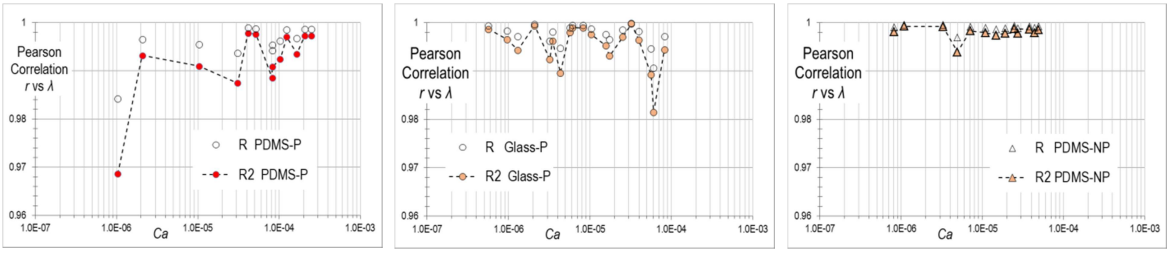

Fig. 9. Values of the Pearson correlation coefficient, R_i and ${R_i}^2$, between flowrate ratio r_i and mobility ratio, λ_i for the entire set of experiments conducted at various Ca_i in the three model pore networks.

We may also attempt to correlate the degree of misalignment with the flow conditions and the two-fluid/network systems. We observe that the $\{\lambda_i, r_i\}_{Ca}$ misalignment from linearity is pronounced in the two periodic networks (PDMS-P & Glass-P) when compared with that of the non-periodic (PDMS-NP), indicating significant presence of end-effects in the periodic networks. The source of the $\{\lambda_i, r_i\}_{Ca}$ misalignment may be attributed to the capillary end-effects that are induced by the relatively stronger role of the menisci – when compared to the effects of the bulk viscosity. Another reason could be the poorer interlacing of the two injected fluids upstream the network flow in the two periodic networks (PDM-P, Glass-P), see Fig. 1. On the contrary, the single entry port of the PDMS-NP network incites a pre-mixture of the two fluids before entering the network. We may also observe that the trends in the ${R_i}^2$, values vs Ca, for the PDMS-P and the Glass-P systems are reversed. That is an interesting behaviour especially considering that the viscosity ratio values are inverse ($\kappa = 1/1.359 = 0.736$ in the PDMS-P and $\kappa = 1.359$ in the PDMS-P system) and the two networks have a different 3D structure.

In the same context, in many diagrams in Fig. 3 pertaining to different constant-Ca experiments, the NWP and WP relative permeability curves intersect at the, so-called, relative permeability crossover flowrate ratio value, $r_x = 1/\kappa$, Eq. (10), indicated by the vertical dashed line. Yet, in some constant-Ca experiments the relative permeability crossover does not coincide with the theoretical value of r_x and that is also observed for the low, ${R_i}^2$, values, ref. Fig. 3 and Fig. **4**

Implementing energy efficiency analysis is another paradigm in characterizing the flow system, in compliance to the normative methodology proposed in [1]. Let us focus on the energy efficiency diagrams in Fig. 8, and, in particular, on the S-curve delineating the critical flow conditions (CFCs) in every two-fluid/network system, Two nominal Ca values may be defined, corresponding to the apex of the two bends of the S-curve, whereby the flow character changes as Ca is increased, from capillary to mixed capillary/viscous and

then to viscous. These nominal values in Ca can be detected graphically or analytically, by setting the 2nd derivative, $\mathrm{d}^2(\log \hat{r}^*)/\mathrm{d}Ca^2 = 0$ and solving for Ca. That of course comes at the extra cost of extensive measurements at various flow conditions to extract the CFCs. Yet, it is possible to follow the path of critical flow conditions, in order to reduce the number of measurements. As discussed in [7] (ref. Fig. 3), along the CFCs, uncertainties associated with measurement errors is minimized and specificity is maximized – that is mainly attributed to the structure of the f_{EU} expression, Eqs. (11) or (18). Tracking the measurements along the CFCs path increases the effectiveness of the SCAL analysis by providing more accurate /unbiased information per unit measurement cost.

Please note that no sophisticated technology is needed to implement the proposed methodology. The measurements of pressure and volumetric fluxes are conventional, taken outside the pore network or natural core.

Moreover, the same, ex-core measurements are used to reveal the IDCP curve, which is essentially the backbone of the flowrate dependency description, Eq. (12), of the two-fluid and core system. The form of the IDCP curve provides valuable information in assessing the extent of end-effects and in deciphering the characteristics of the interstitial flow structure. Another convincing paradigm on how the IDCP curve may be used as a forensic tool in revealing the structure of the interstitial flow is provided in the systematic SCAL study performed on a core of natural Clasach sandstone [2]. An analysis of the measured relative permeabilities, similar to that described in paragraph 4.1, revealed a sharply decreasing intrinsic dynamic capillary pressure function, $A(\log Ca)$, over moderate- to /high-Ca flow conditions. That seemed to be contradicting the smooth, asymptotic transition to zero ($\log A \to 0$) depicted in Fig. 7. Nevertheless the sharp decrease of A at moderate/high-Ca flow conditions was an indication of a sharp reduction of capillary resistances. The particular structure of the IDCP curve, indicates the onset of emulsification at high-Ca flowrates. This interstitial flow characteristic was revealed from ex-core measurements and that particular case indicates the forensic capabilities of the IDCP curve.

In the current study the trend in the revealed IDCP functions, depicted in Fig. 7, is consistent to video observations. The interstitial flow structures comprise mixtures of connected WP and intermittent flows of disconnected NWP fluidic elements; the latter are separated from the WP through n/w menisci remaining in contact to the pore walls; no signs of emulsification were observed.

In addition, the generalized specific characteristic invariants, pertaining to the two-fluid and pore network flow system, i.e. the locus of Critical Flow Conditions, the locus of cross-over relative permeability conditions, as well as the Intrinsic Dynamic Capillary Pressure curve, can be used as flow system identities and that could be a strong tool in developing flow system characterization ("rock-typing") methodologies and techniques.

In the reservoir engineering domain, the ability to handle a functional form of the relative permeabilities, accounting for true-to-mechanism flowrate dependency, through the IDCP curve, can definitely improve the specificity of field-scale simulators, or increase the efficiency in machine learning interventions. The energy efficiency based analysis can be a powerful tool in assessing the operational efficiency of enhanced oil recovery or CO_2 sequestration interventions, extending the energy transition timelines of such energy intensive activities.

As per future research, the outcome of the current study advocates the deployment of similar lab study in artificial or natural cores.

M.V. acknowledges support from the German Academic Exchange Service (DAAD-5752335 Research Stays for University Academics and Scientists, 2024) and from the Univ. of West Attica for his sabbatical leave.
K.M. acknowledges support from Erasmus+ Short term placement mobility.
H.S. and N.K. would like to thank the Deutsche Forschungsgemeinschaft (DFG, German Research Foundation) for supporting this work by funding SFB 1313, Project Number 327154368.. HS acknowledges funding by the DFG under Germany's Excellence Strategy - EXC 2075 - 390740016.

References

1. Valavanides, M.S. TiPM **123** (1), https://doi.org/10.1007/S11242-018-1026-1 (2018)
2. Valavanides, M.S., Mascle, M., Youssef, S., Vizika, O. E3S Web of Conferences **146**, 03002, https://doi.org/10.1051/e3sconf/202014603002 (2020)
3. N. Karadimitriou, M.S. Valavanides, K. Mouravas, H. Steeb, Petrophysics **64** (5), https://doi.org/10.30632/PJV64N5-2023a4 (2023)
4. M.S. Valavanides, Oil & Gas Science and Technology - Rev. IFP Energies nouvelles **73** (6), https://doi.org/10.2516/ogst/2017033 (2018)
5. M.S. Valavanides, TiPM **150**, https://doi.org/10.1007/s11242-023-02012-5 (2023)
6. O. Aursjo, M. Erpelding, K.T. Tallakstad, E.G. Flekkøy, A. Hansen, K.J. Maloy, *Frontiers in Physics* **2**(63), 1-9. DOI: 10.3389/fphy.2014.00063 (2014)
7. M.S. Valavanides, E. Totaj, M. Tsokopoulos, , *Journal of Petroleum Science and Engineering* **147**, 181-201, DOI: 10.1016/j.petrol.2016.04.039 (2016)
8. Y. Jh Xia, G.M. Whitesides, Annual Review of Materials Science **28**, 153-184. DOI: 10.1146/annurev.matsci.28.1.153 (1998)
9. A. Yiotis, L. Talon, D. Salin, *Phys. Rev* E **87**, 033001 (2013), https://doi.org/10.1103/PhysRevE.87.033001